33RD CONGRESS
OF THE INTERNATIONAL COUNCIL
OF THE AERONAUTICAL SCIENCES
STOCKHOLM, SWEDEN, 4-9 SEPTEMBER, 2022

ICAS
2022
SWEDEN

INVESTIGATION OF TWO-DIMENSIONAL VORTEX DYNAMICS IN THE V103 CASCADE

Yihan Zhao[1], Yang Liu[1], Shuaichen Zhu[1], Hongyi Xu[1] & Duo Wang*[1]

[1]Department of Aeronautics and Astronautics, Fudan University, Shanghai, China

Abstract

Aeroengine has always been a focus in aerospace engineering. With the continuous demanding to improve the engine performance, it is crucial to investigate the complex flow structures in cascades, such as the flow separation, vortex generations and turbulent phenomenon. The two-dimensional incompressible flow in the V103 cascade was investigated by the direct numerical simulations (DNS). The detailed instantaneous flow structures with different Reynolds numbers (*Re*) were obtained. Focusing on the vortex structures and dynamics, the paper applied the newly defined vortex identification (VI) method, namely Rortex, to successfully calculate the rigid-rotation of fluid particles, and therefore precisely capture the vortices in a V103 cascade. The evolutions of vortices and their effects on the blade aerodynamical coefficients were investigated. The coefficient spectra with multi-frequency harmonics were found relating to the periodic appearances of low-pressure zones in the flow separation regions. Resulted by the vortex sheding, these low-pressure zones presented more complex distribution patterns with the increase of *Re*, which generated more sub-harmonics in the spectra of aerodynamical coefficients for higher *Re* cases. Furthermore, the *R-S* decomposition and the vorticity transport equation were applied to explain the vortex generation mechanisms in the shear layers along the V103 blade surfaces. The vortex characteratics were investigated by the vortex cores in both strong and weak shear regions and the formation mechanisms were explained by the governing equation. The findings provides the engineering community with a more physically in-depth understanding of the corresponding vortex structures and their interactions in the V103 cascade.

Keywords: Direct numerical simulation; Vortex shedding; Rotex; Vortex dynamics

1. Introduction

As the core component of an flight vehicle, aeroengine is a focal topic in the entire history of aviation development. The aeroengine technology significantly impacts the progress of aviation industry. The performance of cascade in the compressor and turbine directly determines the capability of the aeroengines. When air flowing through the cascade, numerous flow phenomenon can be observed, such as flow separation and vortices [1]. Therefore, the detailed studies of the complex flow structures in a cascade have become an important research content to improve the performance of aeroengines, especially for the stable operation of compressor and the energy loss of turbomachinery, which mainly relate to the vortex evolution process and its generation mechanism. To deeply investigate the topic, researchers focus on the structures and dynamics of the cascade flow for a long time and make many important achievements [2].

The flows in a compressor cascade are mainly studied by the experiments or numerical simulations. For experimental investigations, Zambonini et al. [3] combined Particle Image Velocimetry (PIV) with the Proper Orthogonal Decomposition (POD) techniques to reveal the inherent unsteady characteristics in the cascade corner regions. The research also exhibited the strong unsteadiness, instability, and complex topological structure of the flow in the separation zone. Koca et al. [4] applied smoke-wire experiments and hot-film experiments to study the relationship between the aerodynamic properties and vortex shedding from the suction surface and the wake of wind turbine blade. However, these experiments are limited by the precision of the experimental methods and the measuring instruments. Such as the tracer particles in PIV technology remarkably affect the flow field measurement, and the resulting image analysis also has interference factors. The complete flow field information is also hard to obtain, especially for the velocity derivatives, which closely relates to describing vortices quantitatively. These are the major difficulties in capturing the detailed space-time evolution process of vortex systems via experimental methods.

Meanwhile, the progress of computational fluid dynamics (CFD) provides supports for understanding the complex flow phenomena in cascade at lower *Re*. In terms of numerical simulations, Sajadmanesh et al. [5,6] used Unsteady Reynolds Averaged Navier Stokes (URANS) equations and POD technology to study flow separation and reattachment on the suction surface of turbine blades. Different vortex modes and vortex evolution processes were also proposed and described on the suction side of low-pressure turbine blades through their further studies based on the large eddy simulation (LES). ZAKI et al. [7,8] applied direct numerical simulation (DNS) to describe flow processes such as flow separation (bypass transition) in the V103 cascade.

Among the numerical simulation investigations, the accuracy of RANS simulations depends on the constitutive equations. The isotropic turbulent models cannot satisfy the anisotropic physical nature of the flow near the wall and corners. The LES and DNS results without the turbulent closure models can capture more sophisticated structures, such as the secondary flows, which are appropriate for investigating the flows with simple configuration and relative lower *Re*. However, limited by the computational resource requirements, the studies of cascade applying LES and DNS are insufficient. For the study of V103 cascade, Wang et al. [9] and Zhu et al. [10] mainly investigated the boundary layer separated flow transition process and the vortex structure of the V103 cascade channel, but there was no quantitative analysis of its generation mechanism. At present, there are still few studies on the flow physical details in the V103 channels, and the dynamic analysis of the vortex separation is scarce. For the vortex identification in the cascade channels, Q criterion was widely applied. A recent study presented the drawbacks of Q-criterion by showing a part of shear being mixed in it [11]. Therefore, the present studies applied the rigid rotating part of fluid, namely the Rortex, to quantitatively describe vortices proposed by Liu [12].

In the paper, the two-dimensional incompressible flow in the V103 cascade was simulated by solving the Navier-Stokes equations with the finite-volume method. The state-of-the-art vortex identification quantity of Rortex is utilized to visualize these transient vortical structures. The *Re* were set at 5000 and 148000 respectively for the numerical simulation. The vortex evolution process and their effects on the blade lift and drag coefficients were investigated. The present studies indicate that the Rortex can be applied to precisely identify the vortex patterns, particularly in the near-wall shear layers, and clearly reveal the two-dimension complex vortex structures on both suction and pressure surfaces of the V103 blade. Moreover, the present investigations provide an in-depth understanding of vortex generating mechanism and their dynamics in the V103 cascade.

2. Mathematical Model and Numerical Methods

The research applied the two -dimensional incompressible N-S equations in the numerical simulation and the non-dimensional governing equations can be written as

$$\frac{\partial u}{\partial x}+\frac{\partial v}{\partial y}=0 \tag{1}$$

$$\frac{\partial u}{\partial t}+\frac{\partial uu}{\partial x}+\frac{\partial uv}{\partial y}=-\frac{\partial P}{\partial x}+\frac{1}{Re}(\frac{\partial^2 u}{\partial x^2}+\frac{\partial^2 u}{\partial y^2}) \tag{2}$$

$$\frac{\partial v}{\partial t}+\frac{\partial uv}{\partial x}+\frac{\partial vv}{\partial y}=-\frac{\partial P}{\partial y}+\frac{1}{Re}(\frac{\partial^2 v}{\partial x^2}+\frac{\partial^2 v}{\partial y^2}) \tag{3}$$

where, u is the non-dimensionless x-component velocity; v is the non-dimensionless y-component velocity; P is the non-dimensionless pressure; Re represents the Reynolds numbers. The non-dimensionless referred pressure P_{inlet} is zero at the inlet. The inflow velocity *U* and blade chord

length *C* are selected as the characteristic velocity and length respectively. The *Re* are 5000 and 148000 in the simulations.
The V103 blade is selected, and the geometric parameters are consistent with the studies of Zaki [7] in the simulations. The V103 compressor is composed of NACA65 blade profile, which is taken from the middle section of stator of a high-load axial compressor in engineering applications. The computational domain is shown in Figure 1. The free flow velocity and the horizontal plane is angled at 42°.

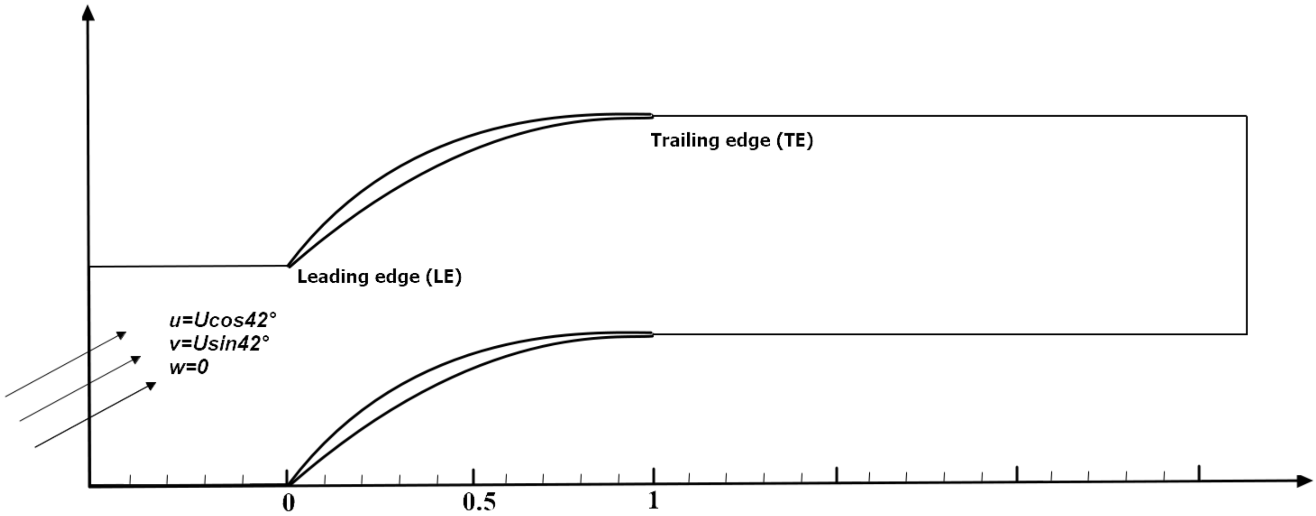

Figure 1 – Schematical drawing of computational domain.

The numerical simulation domain and the grid are shown in Figure 2. the mesh in the computation domain is 661×258. The vortex shedding process contains small scales vortices near the trailing edge of the blade and the mesh were refined at the both leading edge and the trailing edge with 360 grids arranging along the blade surface in streamwise. The minimum distance between the firdt meshes and blade surface are 7.7×10^{-5} and 7.6×10^{-5} for the pressure and suction sides respectively, and the time step is equally set at $\Delta t=5\times10^{-5}$ and $\Delta t=4\times10^{-5}$ for *Re*=5000 and 148000 cases.

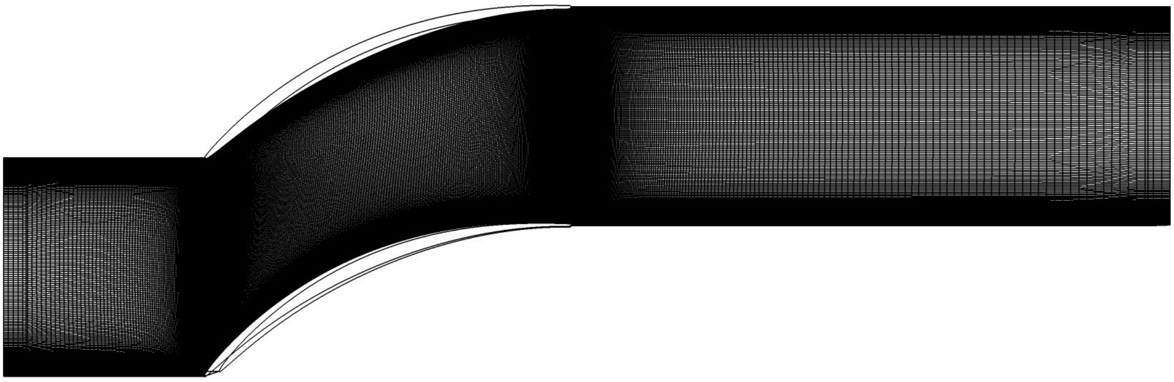

Figure 2 – The mesh distribution in the computation domain

The meshes and the time-step were found being able to provide a stable computation for the entire calculation, and the total number of time steps was 1.2×10^{6} and 7.65×10^{5}. The DNS solutions are converged to the machine accuracy at each time step, which guaranteed the solutions satisfies the conservation of mass and momentum. The velocity boundary conditions on the inlet and outlet are set as the Dirichlet and Neumann conditions, and the pressure boundary conditions are Neumann on both the inlet and outlet. The no-slip boundary conditions are used on the blade surface and the rest of the boundaries have periodic boundary conditions. For the numerical simulation techniques, the governing equations are using in the finite volume scheme. The second order Adams-Bashforth explicit advance scheme is applied to discrete the convection terms in the momentums equation and the second order Adams-Moulton implicit scheme are used for the diffusion terms. The fractional step method is applied to decouple the momentum and pressure [13]. The staggered grid method is used in the spatial discretion. and the multi-grid method is applied to guarantee the convergence of the pressure Poisson equation.

For the numerical simulation techniques, the governing equation was discretized in the finite volume scheme. The second order Adams-Bashforth explicit advance scheme was applied to discrete the convection terms in the momentum equation and the second order Adams-Moulton implicit scheme is used for the diffusion terms. The fractional step method was applied to decouple the momentum and pressure. The staggered grid method was used in the spatial discretion. and the multi-grid method is applied to guarantee the convergence of the pressure Poisson equation.

3. Result and discussing

Before the analysis, it is necessary to give the definition of the non-dimension lift and drag coefficients (aerodynamic coefficients) as

$$N=-\int_{LE}^{TE}(p_u\cos\theta+\tau_u\sin\theta)dl_u+\int_{LE}^{TE}(p_l\cos\theta-\tau_l\sin\theta)dl_l \tag{4}$$

$$A=\int_{LE}^{TE}(-p_u\sin\theta+\tau_u\cos\theta)dl_u+\int_{LE}^{TE}(p_l\sin\theta+\tau_l\cos\theta)dl_l \tag{5}$$

$$L=N\cos\alpha-A\sin\alpha \tag{6}$$

$$D=N\sin\alpha+A\cos\alpha \tag{7}$$

$$C_L=\frac{L}{0.5\rho u_0^2C} \tag{8}$$

$$C_D=\frac{D}{0.5\rho u_0^2C} \tag{9}$$

where p_u (τ_u) and p_l (τ_l) are the pressure (unit area shear force) on the suction and pressure surfaces; $(sin\theta,\cos\theta$) is the unit normal vector of the blade surface; N and A are the resultant force of pressure and shear force in the horizontal and vertical directions; L and D are the pressure and shear forces; α is the angle of the free incoming flow and the horizontal direction. C_L and C_D are the lift coefficient and the resistance coefficients.

3.1 *Re*=5000 flow in V103 cascade channel

In the case of small *Re* number (*Re*=5000), as shown in Figure 3, the suction surface generates a relative larger scale separation vortex V1 compared to the higher *Re* cases. Figure 3 presents the vortex shedding process in the cascade for an entire shedding period. The generation of vortex V1 relates to the reverse pressure gradient as seen in Figure 4, which also induces the flow separation. Meanwhile, the pressure difference between the pressure and suction surfaces results in the vortex V2 being generated right behind the the blade trailing edge. The vortices of V1 and V2 are periodically and continuously shedding in a pair pattern to generate the wake vortex streets containing two counter-rotating vortices with approximately equaling rotating strengths. The Rortex quantity clearly identifies V1 in the strong shear layer on the blade suction surface, which provides the capability to investigate more complex vortical structures in the higher *Re* cases with the multiscale vortices being generated inside the shear layer.

Figure 5 presents the instantons lift and drag coefficients of the V103 blade. When the flow is fully developed after a non-dimensional period of 15, the lift and drag coefficients start to oscillate periodically. The time averaged lift coefficient is 0.4965 and the time averaged drag coefficient is 0.1706. Applying the fast Fourier transform (FFT), the spectra of lift and drag coefficients are presented by

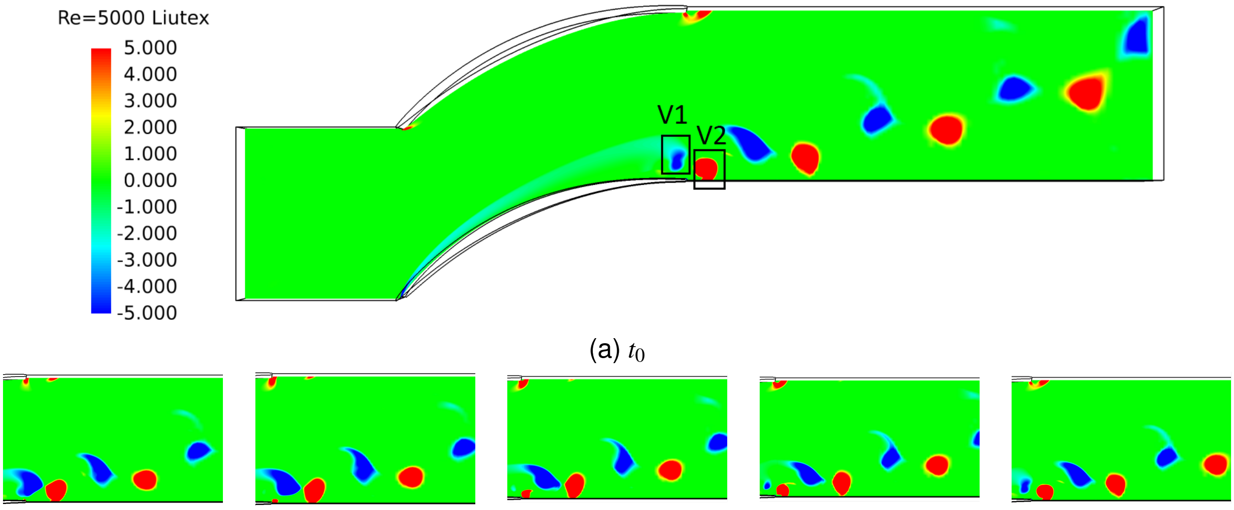

(a) t_0

(b) $t_0 + 1/5T$ (c) $t_0 + 2/5T$ (d) $t_0 + 3/5T$ (e) $t_0 + 4/5T$ (f) $t_0 + T$

Figure 3 – Instantons vortex structures represented by the Rotex magnitude for *Re*=5000 with T being the shedding period and $t_0 = 15.272$.

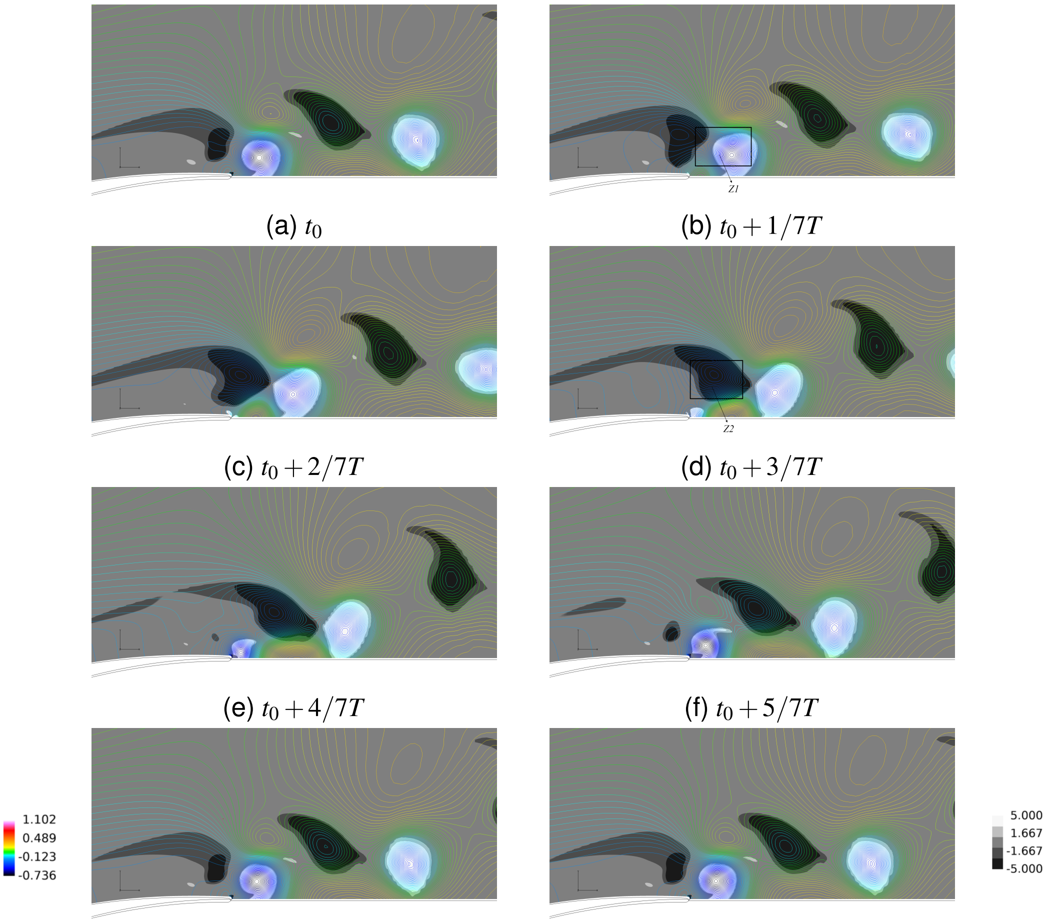

(a) t_0 (b) $t_0 + 1/7T$

(c) $t_0 + 2/7T$ (d) $t_0 + 3/7T$

(e) $t_0 + 4/7T$ (f) $t_0 + 5/7T$

(g) $t_0 + 6/7T$ (h) $t_0 + T$

Figure 4 – Pressure counters and R_z distributions on the suction surface for *Re*=5000 with T being the shedding period.

Figure 6 with a dominant frequency at 2.03712. The dominant frequency precisely corresponds to the shedding frequency of V1 and V2 in Figure 3, indicating that the periodic fluctuations of the lift-drag coefficients are resulted from the shedding of V1 and V2. The Physical mechanism of the time variations of aerodynamic coefficients with the dominant frequency relates to the flow-through area variations of the low-pressure and high-pressure regions on the suction and pressure surface in a shedding period, as explained by Li and Xu [14]. The locations of V1 and V2 cores are also the low-pressure zone in Figure 4. In the entire shedding period, V1 and V2 flow through the region upper the trailing edge of the blade alternately and brings out two adjacent low-pressure zones near the suction surface tail in the wake, as seen Z1 and Z2 in Figure 4. The appearance of each low-pressure zone disturbs the pressure distributions around the blade and results in the fluctuation of lift and drag coefficients with a shorter period. Because these low-pressure zones appear twice in an entire shedding period, the frequency of this fluctuation is twice of the V1 and V2 shedding frequency at 2.03712 and generate the subpeak at 4.01765 in the spectrum harmonics in Figure 6. Moreover, these low-pressure zones locate above the blade tail and has limited influence on the pressure upon the pressure surface. Then, the fluctuation mode with frequency at 4.01765 almost vanish in the spectra of the drag and lift forces acting on the pressure surface.

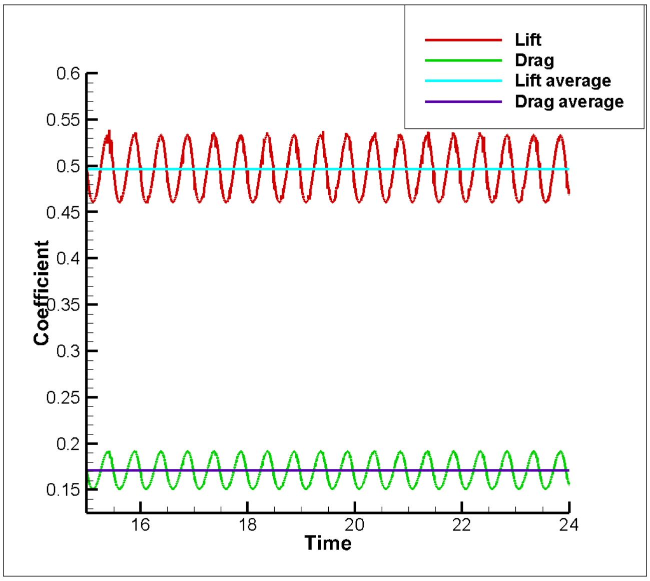

Figure 5 – The instantons lift and drag coefficients in the *Re*=5000 case.

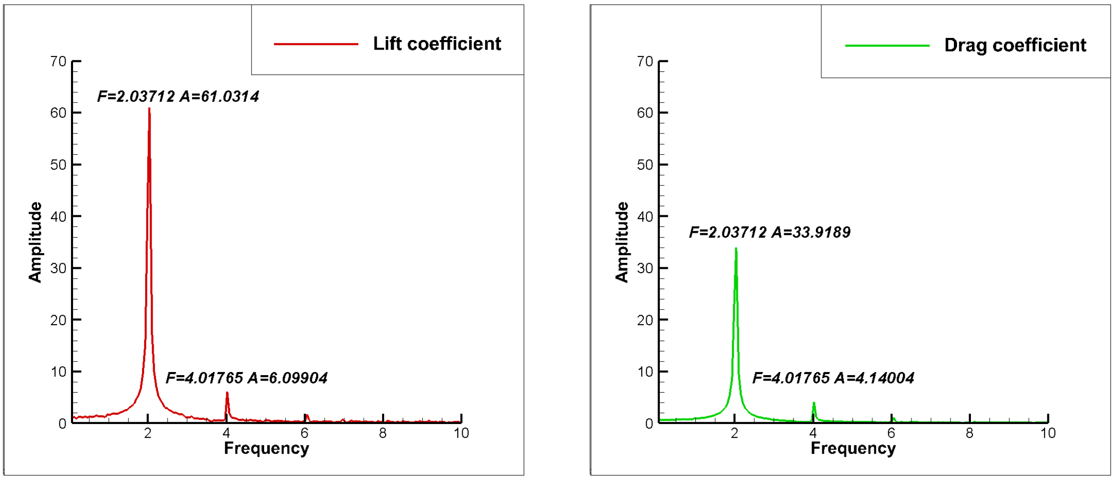

(a)

(b)

Figure 6 – The spectrums of the lift and drag coefficients.

3.2 *Re*=148000 flow in V103 cascade channel

The instantaneous vortical structures are presented in Figure 7 (a-g) in the entire cascade with *Re*=148000. With *Re* increasing, the vortex structures in the cascade become more complex and the flow separation phenomenon can be found at the trailing edge of both the suction and the pressure surfaces [7,8]. Compared to the lower *Re* cases, the starting points of separation vortices on the suction and pressure surfaces approach to the leading edge and the rotating regions of these separation vortices shrinks as presented in Figure 7. The flow separation on the blade suction surface starts at the location of vortex V3 in Figure 7, which is generated periodically. Below the vortex V3, the secondary vortex V4 can be observed with the opposite rotating direction. Behind the first pair vortices of V3 and V4, another pair of vortices V5 and V6 are found. There is also a larger size vortex V7 shedding downstream the V6 vortex. V3-6 present the vortex pair string along the blade suction surface. In the process of these vortex evolutions, as shown in Figure 7(b), the vortex V8 is the initial vortical structures generated by the reverse pressure gradient from the separation starting point. Reshaped by the strong shear in the main flow, the vortex V3 is divided into two vortices, and one of the vortices, i.e. V3, merges with V5, and enhances the V5 rotating strength. As shown in Figure 7(c), the vortex V5 is restricted by the main flow and has the dominant effect on V6, which results in V6 being deformed and divided into two vortices of V9 and V10. At the time instant $t_0 + 0.405$ in Figure 7(d), V9, V10 and V7 generates a vortex package of V11 as they moves to downstream. The vortex V10 in the package V11 dissipates as the flow developing. Meanwhile, a string of vortices is generated by the flow separation on the pressure surface, which meets and co-rotates with V9 and V7 behind the suction surface tail and eventually forms a vortex package of V12 in the wake, as seen in Figure 7(a) and Figure 7(f). The similar flow structure of vortex package V7 was also reported by Pauley, Moin, Haitao et.al [15].

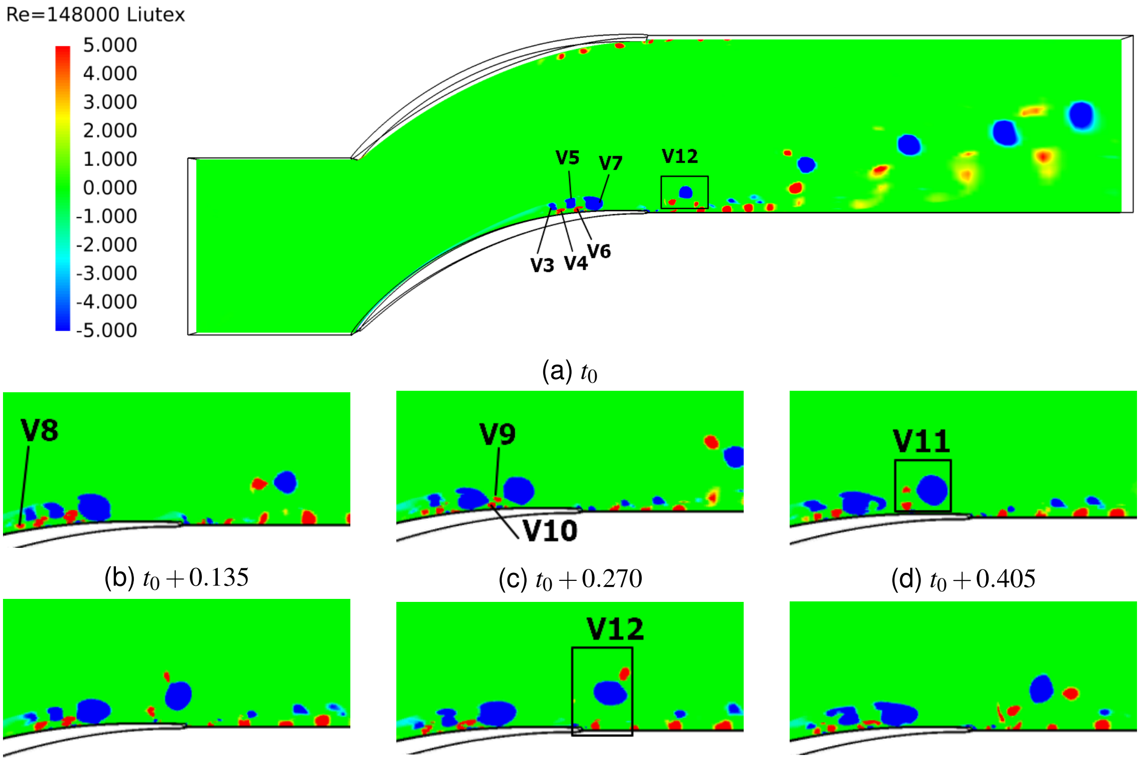

(a) t_0

(b) $t_0 + 0.135$

(c) $t_0 + 0.270$

(d) $t_0 + 0.405$

(e) $t_0 + 0.540$

(f) $t_0 + 0.675$

(g) $t_0 + 0.810$

Figure 7 – Instantaneous vortical structures identified by the Rortex magnitude for the *Re*=148000 case with $t_0 = 15.284$ (a): the vortices in the V103 cascade channel; (b)-(g): the evolution process of the vortices on the suction surface in an entire shedding period.

Figure 8 illustrates the FFT specta of the lift and drag coefficients for the *Re*=148000 case. The shedding frequency of vortices is generally higher than the lower *Re* case. The spectrum presents

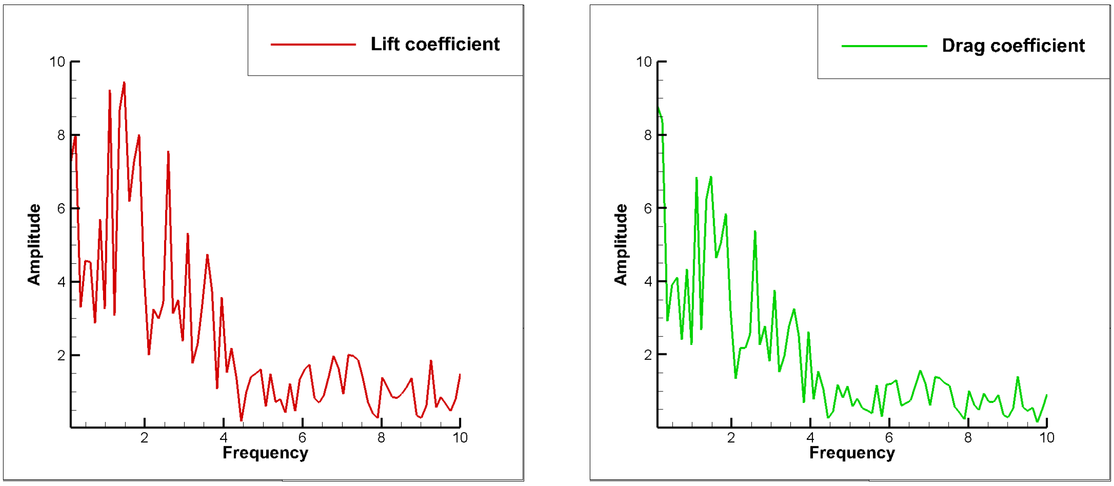

(a) (b)

Figure 8 – Lift and drag coefficient spectrum of the V103 blade for the case of *Re*=148000 case.

a series of sub-harmonics, which is resulted from the more complex vortices shedding regime with a series of vortices being generated on both the pressure and suction surfaces as abovementioned. For a fixed location on the suction surface tail, V3-7 approach to the location sequentially and bring out a low-pressure regions near the location several times in an entire shedding period. These low-pressure regions of V3-7 fluctuate the pressure on the locally, which also oscillate the force acting on the location. The curvature of blade surface is different at each location, then the local force fluctuations cannot be balanced mutually and results in the oscillations of the total force with shorter periods. Therefore, a series of sub-harmonics can be observed in the lift and drag coefficient spectra. Similarly with the force acting on the suction surface, the vortex string under the pressure surface tail can also fluctuate the total force acting on the pressure surface with the frequency compared to the entire shedding frequency.

3.3 Analysis of the vortex dynamics

For the incompressible flow, the vorticity ω transport equation can be written as

$$\frac{D\omega}{Dt} = \nabla v \cdot \omega + \frac{1}{Re}\Delta\omega \tag{10}$$

Based on the ***R-S*** decomposition in [16], the vectors of ***R*** and ***S*** denote the rigid rotation (Rortex) and the shearing motion (Shear), respectively, and the vector of Shear (***S***) can then be calculated by

$$\vec{S} = \vec{\omega} - \vec{R} \tag{11}$$

Applying the vorticity ω transport equation and the *R*-*S* decomposition, the dynamic equation of *R* can be written as [17]

$$\frac{DR}{Dt} = \lambda_r R + \lambda_r c_r l_r - \lambda_r Real(c_c l_c) - 2\lambda_{ci} Image(c_c l_c) - \frac{DS}{Dt} + \frac{1}{Re}\Delta\omega \tag{12}$$

where λ_r is the real eigenvalue of the velocity gradient tensor ($\nabla\vec{v}$) for the normalized eigenvector l_r and $\lambda_{cr} \pm i\lambda_{ci}$ are the complex eigenvalues with the eigenvectors l_c and $\bar{l}_c$, the linear expression based on these eigenvectors is

$$S = c_r l_r + c_c l_c + \overline{c_c l_c} \tag{13}$$

In the present studies, the flow is two dimensional, $\lambda_r \equiv 0$ and the rotation direction, as well as the vorticity, is always in the *z*-axis. Therefore, c_c=0 and the above *R* dynamic equation Equation.12 can be simplified as

$$\frac{DR_z}{Dt} = -\frac{DS_z}{Dt} + \frac{1}{Re}\Delta\omega_z \tag{14}$$

Under the Lagrangian framework, the rotating strength presented by R_z is governed by terms of $\frac{DS_z}{Dt}$ standing for the shear effect and $\frac{1}{Re}\Delta\omega_z$ providing the viscous effect.

Applying the budget analysis of Equation.14 at the vortex regions of V3-6, the viscous effect $\frac{1}{Re}\Delta\omega_z \approx 0$ is small, as seen in Table 1. The vortices V3-6 are mainly contributed by the shearing term $\frac{DS_z}{Dt}$,which quantitively indicates the generation of separation vortices comes from the shear effect. Under the Lagrangian framework, the above discussions suggest that $\frac{DR_z}{Dt} + \frac{DS_z}{Dt} = \frac{1}{Re}\Delta\omega_z \approx 0$ and $\tilde{\omega}_z = \tilde{R}_z + \tilde{S}_z \approx \mathrm{constant}$ where $\tilde{f}$ denotes the physical quantity under the Lagrangian framework. Thereby, the shear $\tilde{S}_z$ has the opposite varying tendency to the rotation $\tilde{R}_z$. With the vortices appearing, $\tilde{R}_z$ will increase or decrease depending on the rotation direction and $\tilde{S}_z$ will decrease or increase corresponding to $\tilde{R}_z$. Then, two the distribution characters of $\tilde{S}_z$ and $\tilde{R}_z$ can be explained, as seen in Figure 9. Firstly, for two nearby points around the outer region of vortices with equivalent vorticity magnitudes, one of the point could move into the rotating region and $\left|\tilde{S}_z\right|$ the decrease with the increase of $\left|\tilde{R}_z\right|$, but the other point stays in the vortex outer regions with a larger $\left|\tilde{S}_z\right|$ inherited from the vorticity magnitude when these points start to separate. Therefore, the strong shear strips can be found around the outer region of vortices as illustrated by Z3-Z5 and vortex cores are usually the weak shear regions. Secondly, as presented by V13 evolving from $t_0 + 0.405$ to $t_0 + 0.540$, the positive $\tilde{S}_z$ is descent with the enhancement of rotating strength $\tilde{R}_z$, and the strong $\tilde{S}_z$ in V13 among the shear layer in Figure 9 (c) will vanishes to generate a weak shear region eventually with V13 developing to a larger vortex.

Table 1 – The distributions of $\frac{DR_z}{Dt}$, $\frac{DS_z}{Dt}$and $\frac{1}{Re}\Delta\omega_z$ at the vortex cores of V3-6 in Figure 7 (a).

	DR_z/Dt	$-DS_z/Dt$	$\lvert\Delta\omega_z/Re\rvert$
V3 core	-278.2	-267.5	$<10^{-2}$
V4 core	224.5	231.1	0.01
V5 core	-669.5	-681.3	$<10^{-2}$
V6 core	624.2	657.1	$<10^{-2}$

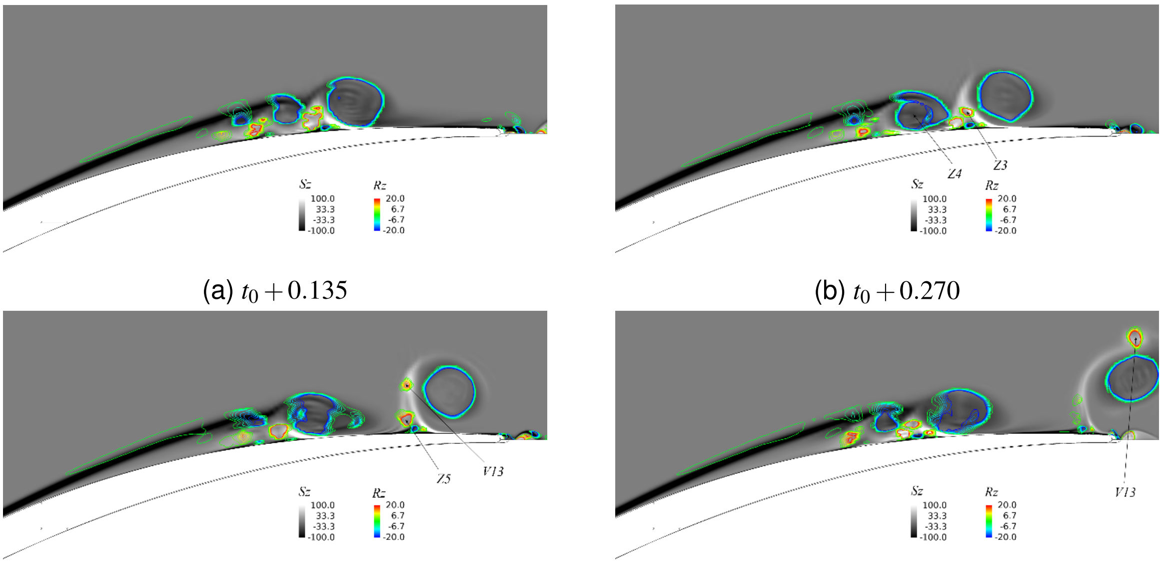

(a) $t_0 + 0.135$

(b) $t_0 + 0.270$

(c) $t_0 + 0.405$

(d) $t_0 + 0.540$

Figure 9 – The distributions of R_z and S_z at each time instants near the V103 suction surface tail for the *Re*=148000 case.

4. Conclusion

The present studies indicate that the Rortex can be applied to precisely identify the vortex structures in the strong shear regions, and clearly reveal the two-dimension complex vortex structures on both the suction and pressure surfaces of the V103 blade. In the case of low *Re*, the dominant frequency precisely corresponds to the shedding frequency of vortices, indicating that the mainly periodic fluctuations of the lift-drag coefficients are generated by the wake vortex shedding. Besides the dominating peak in the coefficient spectra, the serval sub-peaks can be observed relating to the higher frequency sub-harmonics. These sub-harmonics are generated by the alternatively appearances of different vortex core low-pressure zones at the adjacent region in an entire shedding period, and the blade surface pressure distribution are disturbed several times by the appearance of low-pressure zones to generate higher frequency fluctuations. With increasing *Re*, the separated vortices present more complex shedding regimes both on the pressure and suction surfaces, and the numbers of the vortices are also increased. Then, as a result, the low-pressure zones generated by these vortices bring more pressure fluctuations in an entire shedding period, and more higher frequency sub-harmonics can be found in the aerodynamical coefficients spectra for the higher *Re* cases. Moreover, in the shear layers of the V103 blade surfaces, the vortex generation mechanisms can be explained by applying the *R-S* decomposition and the vorticity transport equation. The vortex characteristic patterns can be observed in both the strong shear region around vortices and the weak shear region at the vortex cores. The generation mechanisms are explained by the governing equation of R_z. The present investigations provide an in-depth understanding of the vortex structures and their dynamics in the V103 cascade.

5. Copyright Statement

The authors confirm that they, and/or their company or organization, hold copyright on all of the original material included in this paper. The authors also confirm that they have obtained permission, from the copyright holder of any third party material included in this paper, to publish it as part of their paper. The authors confirm that they give permission, or have obtained permission from the copyright holder of this paper, for the publication and distribution of this paper as part of the ICAS proceedings or as individual off-prints from the proceedings.

6. Acknowledgments

The research was funded by the Shanghai Municipal Science and Technology Commission of China (no. 20JC1413700) and the Shanghai Municipal Education Commission of China (no. AR960).

References

[1] Zheng X Q, Zhou X B and Zhou S.Investigation on a type of flow control to weaken unsteady separated flows by unsteady excitation in axial flow compressors. Journal Of Turbomachinery-Transactions Of The Asme, Vol. 127,No. 3, pp 489-496,2005.

[2] Chen H and Tan C. Review Of Investigation Into Internal Flow Of Turbomachinery. Chinese Journal Of Mechanical Engineering, Vol. 43 No. 2, pp 1-12,2007.

[3] Zambonini G, Ottavy X and Kriegseis J. Corner separation dynamics in a linear compressor cascade.Journal Of Fluids Engineering-Transactions Of The Asme, Vol. 139,No. 6,2017.

[4] Koca K, Genc M S, Acikel H H, Cagdas M, Bodur T M. Identification of flow phenomena over NACA 4412 wind turbine airfoil at low Reynolds numbers and role of laminar separation bubble on flow evolution. Energy, Vol. 144,pp 750-764,2018.

[5] Sajadmanesh S M, Mojaddam M, Mohseni A, Nikparto A.. Numerical identificaticin of separation bubble in.an ultra-high-lift turbine cascade using URANS simulation and proper orthogonal decomposition. Aerospace Science And Technology, Vol. 93,2019.

[6] Sajadmanesh S M, Mohseni A, Mojaddam M. Vortex dynamics mechanisms of separated boundary layer in a highly loaded low pressure turbine cascade. International Journal Of Heat And Fluid Flow, Vol. 82,2020.

[7] Zaki T, Durbin P, Wissink J, Rodi W. Direct numerical simulation of by-pass and separation-induced transition in a linear compressor cascade. Proceedings Of The Asme Turbo Expo 2006, Vol 6, pp 1421-1429,2006.

[8] Zaki T A, Wissink J G, Durbin P A, Rodi W. Direct computations of boundary layers distorted by migrating wakes in a linear compressor cascade. Flow Turbulence Combustion,Vol. 83 No. 3, pp 307-322, 2009.

[9] Wang M Y, Li Z L, Yang C W, Han G, Zhao S F, Lu X G. Numerical investigations of the separated transitional flow over compressor blades with different loading distributions. Aerospace Science And Technology, Vol. 106 2020.

[10] Zhu H, Li Y. High order direct numerical simulation of compressor cascade channel . Journal of Aerospace Power,Vol. 35,No. 6,pp 1286-1295,2020.

[11] Liu C, Gao Y, Tian S, Dong X. Rortex: a new vortex vector definition and vorticity tensor and vector decompositions. Phys Fluids,Vol. 30 No. 3, 2018.

[12] Liu C. Liutex and Third Generation of Vortex Identification Methods.Acta Aerodynamica Sinica, Vol. 38 No. 3, pp 413-431,2021.

[13] Kim J, Moin P. Application of a fractional-step method to incompressible Navier-Stokes equations. Journal Of Computational Physics, Vol. 59, No. 2, pp 308-323, 1985.

[14] Li M,Xu H.Investigation Of Aerodynamic Interactions Between NACA0012 Airfoils In Tandem.32nd Congress of the International Council of the Aeronautical Sciences,Shanghai,China,2021.

[15] Pauley L L, Moin P and Rsynolds W C. The structure of two-dimensional separation. Journal Of Fluid Mechanics,Vol. 220, pp 397-411,1990.

[16] Wang Y, Gao Y, Liu J, Liu C.Explicit formula for the Liutex vector and physical meaning of vorticity based on the Liutex-Shear decomposition.Journal Of Hydrodynamics, Vol. 31 No. 3, pp 464-474,2019.

[17] Wang D, Liu Y, Li H, Xu H.Secondary instability of channel-confined transition around dual-circular cylinders in tandem. International Journal Of Mechanical Sciences, Vol. 208,2021.